

# Self-Assembly of Spinel Nanocrystals into Mesoporous Spheres as Bifunctionally Active Oxygen Reduction and Evolution Electrocatalysts

Dong Un Lee,<sup>[a]</sup> Jingde Li,<sup>[a]</sup> Moon Gyu Park,<sup>[a]</sup> Min Ho Seo,<sup>[b]</sup> Wook Ahn,<sup>[a]</sup> Ian Stadelmann,<sup>[a]</sup> Luis Ricardez-Sandoval,<sup>\*[a]</sup> and Zhongwei Chen<sup>\*[a]</sup>

The present work introduces spinel oxide nanocrystals self-assembled into mesoporous spheres that are bifunctionally active towards catalyzing both the oxygen reduction reaction (ORR) and the oxygen evolution reaction (OER). The electrochemical evaluation reveals that (Ni,Co)<sub>3</sub>O<sub>4</sub> demonstrates a significantly positive-shifted ORR onset and half-wave potentials [−0.127 and −0.292 V vs. saturated calomel electrode (SCE), respectively], whereas Co<sub>3</sub>O<sub>4</sub> results in a negative-shifted OER potential (0.65 V vs. SCE) measured at 10 mAcm<sup>−2</sup>. Based on

the DFT analysis, the potential at which all oxygen intermediate reactions proceed spontaneously is the highest for (Ni,Co)<sub>3</sub>O<sub>4</sub> ( $U=0.66$  eV) during ORR, whereas it is the lowest for Co<sub>3</sub>O<sub>4</sub> ( $U=2.09$  eV) during OER. The high ORR activity of (Ni,Co)<sub>3</sub>O<sub>4</sub> is attributed to the enhanced electrical conductivity of the spinel lattice, and the high OER activity of Co<sub>3</sub>O<sub>4</sub> is attributed to relatively weak adsorption energy promoting rapid release of evolved oxygen.

## Introduction

Soaring energy demands during the past few decades have led to continued burning of fossil fuels, producing greenhouse gases that contribute to increasing global warming. To address the energy demands and reduce carbon emissions, advanced energy-storage conversion and storage systems that produce energy in a clean and sustained fashion have recently been investigated by many researchers. Rechargeable metal–air batteries are considered one of the most promising future energy systems owing to their extremely high energy densities and flat discharge potentials.<sup>[1]</sup> These advantages of rechargeable metal–air batteries make them particularly interesting for applications in electric vehicles to improve the insufficient driving range, as well as in electrical-energy storage (EES) systems for coupling intermittent renewable wind- and solar-energy sources into smart energy grids.

Rechargeable metal–air batteries, however, require active bifunctional electrocatalysts to accelerate the kinetics of the intrinsically sluggish oxygen reduction reaction (ORR) and oxygen evolution reaction (OER), which are the fundamental electrochemical reactions that govern the discharge and charge processes, respectively.<sup>[2]</sup> For the development of practically viable rechargeable metal–air batteries, bifunctional electrocatalysts residing in the air electrode must be sufficiently catalytically active towards both ORR and OER.<sup>[3]</sup> Currently, the state-of-the-art catalyst, platinum on carbon (Pt/C), demonstrates the highest ORR activity. However, it is very costly owing to its scarcity, and is only monofunctionally active towards ORR, making it unsuitable for the production of cost-competitive rechargeable metal–air batteries.<sup>[4]</sup> For instance, primary (non-rechargeable) zinc–air batteries are the only type of metal–air battery that is currently available on the market for niche applications such as hearing aids, and it utilizes inexpensive earth-abundant Mn-based catalysts. Despite their affordability and excellent discharge characteristics, primary zinc–air batteries cannot be recharged efficiently owing to insufficient OER activity (charge performance) of the catalyst.

Recently, numerous non-precious bifunctional catalyst developments have been reported in the literature, including transition-metal oxides,<sup>[5]</sup> nanostructured carbons,<sup>[6]</sup> and hybrid catalysts.<sup>[7]</sup> For example, a new metal-free transition-metal oxide such as mesoporous Co<sub>3</sub>O<sub>4</sub>, synthesized by silica templating, was shown to be highly active and durable as a bifunctional catalyst, demonstrating a similar total overpotential of 1.034 V and superior methanol-tolerance compared to its noble-metal counterparts.<sup>[5a]</sup> Nanostructured carbon-based catalysts were also developed; Tian et al. reported coaxial nanocables with surface nitrogen groups that are capable of catalyzing both

[a] D. U. Lee, Dr. J. Li, M. G. Park, Dr. W. Ahn, I. Stadelmann, Prof. L. Ricardez-Sandoval, Prof. Z. Chen  
Department of Chemical Engineering  
Waterloo Institute for Nanotechnology  
Waterloo Institute for Sustainable Energy  
University of Waterloo  
200 University Avenue West, Waterloo ON N2L 3G1 (Canada)  
E-mail: lricardezsandoval@uwaterloo.ca  
zhwchen@uwaterloo.ca

[b] Dr. M. H. Seo  
Hydrogen & Fuel Cell Center  
New & Renewable Energy Research Korea Institute of Energy Research (KIER)  
20-41, Sinjaesaengeneogi-ro, Haseo-myeon, Buan-gun, Jellabuk-do, 56332 (South Korea)

Supporting Information and the ORCID identification number(s) for the author(s) of this article can be found under <https://doi.org/10.1002/cssc.201700369>.

ORR and OER with significantly reduced overpotentials for both oxygen reactions.<sup>[6a]</sup> Recently, hybrid catalysts composed of non-precious metal oxides and nanocarbons have received tremendous attention owing to their improved catalytic activity through synergistic enhancements between the two components. Notably, nitrogen-doped carbon nanotubes decorated with Co<sub>3</sub>O<sub>4</sub> nanocrystals were shown to be bifunctionally effective for rechargeable zinc–air batteries, demonstrating stable charge and discharge voltages over a total of 100 h without any voltage degradation.<sup>[8]</sup>

Despite these efforts, much work is still needed in terms of non-precious bifunctional catalyst development to understand the exact reaction mechanisms and degradation pathways of mixed spinel oxides such as NiCo<sub>2</sub>O<sub>4</sub>, MnCo<sub>2</sub>O<sub>4</sub>, and FeCo<sub>2</sub>O<sub>4</sub>. Specifically, the work presented here utilizes both experimental and first-principles DFT computational approaches to investigate the bifunctional electrocatalytic behaviors of spinel-structured oxides of varying compositions, including Co<sub>3</sub>O<sub>4</sub>, (Ni,Co)<sub>3</sub>O<sub>4</sub>, and (Mn,Co)<sub>3</sub>O<sub>4</sub>. These spinel oxides fabricated by a facile solvothermal technique demonstrate a self-assembled mesoporous spherical morphology with varying degrees of catalytic activity towards both ORR and OER, depending on the type of transition metal (Co, Ni, and Mn) inserted into the octahedral sites of the spinel lattice. The first-principles DFT computational method was employed to find the potential at which all oxygen intermediate steps proceed spontaneously to verify the experimentally obtained electrochemical results. The outcome of this study opens the door for designing affordable non-precious bifunctional catalysts with tailored ORR and OER activities depending on the modification of the composition of spinel metal oxides for rechargeable metal–air battery applications.

## Results and Discussion

The mesoporous spheres were synthesized by a facile solvothermal technique using ammonium bicarbonate as precipitation and pore-forming agent to promote the formation of metal-carbonate nanocrystals self-assembled into spherical structures (Figure 1 a). The heat treatment in the presence of oxygen (in air) thermally decomposes metal carbonates into metal-oxide spheres, releasing CO<sub>2</sub> gas and leaving pores behind<sup>[9]</sup> as shown by Equation (1):



in which M is one (or more) transition metal(s) used in this study (Co, Ni and Co, or Mn and Co). The release of CO<sub>2</sub> gas within the spherical metal-oxide phase leaving behind pores is very interesting for enhanced electrocatalysis because it increases the active surface area and facilitates mass transport. The three kinds of porous spinel oxide synthesized in this study, Co<sub>3</sub>O<sub>4</sub>, (Ni,Co)<sub>3</sub>O<sub>4</sub>, and (Mn,Co)<sub>3</sub>O<sub>4</sub> were analyzed by scanning electron microscopy (SEM) to reveal their porous spherical morphology (Figure 1 b–d). Without the addition of ammonium bicarbonate, randomly oriented sheet-like metal-oxide structures of varying sizes were observed (Figure S1 in

the Supporting Information). Further inspection of higher-magnification SEM images of the sphere oxides revealed nanosized crystals that self-assembled into a few micron-scale spherical structures (Figure 1 e–g). Interestingly, despite using the same amount of reagents during the synthesis, including the total amount of transition-metal precursors, slightly different sizes of nanocrystals were observed owing to changes in the crystal-lattice structure with the insertion of Ni and Mn into Co<sub>3</sub>O<sub>4</sub>.

For bifunctional catalysis, high-surface-area materials are desirable because ORR and OER are interfacial reactions that occur on the surface of active catalysts.<sup>[10]</sup> The surface area of the metal oxides was measured by conducting BET analyses, resulting in very high specific surface areas of 132, 66.3, and 162 m<sup>2</sup>g<sup>−1</sup> for Co<sub>3</sub>O<sub>4</sub>, (Ni,Co)<sub>3</sub>O<sub>4</sub>, and (Mn,Co)<sub>3</sub>O<sub>4</sub>, respectively (Figure S2). The nitrogen adsorption–desorption isotherms showed a hysteresis loop in the region of high relative pressure (type IV isotherms) owing to the presence of mesopores formed by interparticle spacing between the nanocrystals. Based on the pore-size distribution obtained by Barrett–Joyner–Halenda (BJH) analysis, the peak pore diameter was found to be 3.6, 12, and 3.5 nm for Co<sub>3</sub>O<sub>4</sub>, (Ni,Co)<sub>3</sub>O<sub>4</sub>, and (Mn,Co)<sub>3</sub>O<sub>4</sub>, respectively, which likely corresponds to the interparticle spacing between nanocrystals of each metal oxide. This mesoporous nature of the spheres is highly beneficial for both ORR and OER because a higher specific surface area increases the number of exposed active sites, and the pores can also act as channels to facilitate rapid mass transport of reactants and products during the catalytic reactions.

The spinel-oxide spheres were analyzed by XRD prior to the thermal decomposition of ammonium bicarbonate, resulting in patterns that closely matched with metal carbonates (PDF #11-0692, Figure 1 h). After heat treatment and release of CO<sub>2</sub>, the XRD patterns of the spheres matched very closely with the typical cubic spinel crystal structure (PDF #74-2120, Figure 1 i). Interestingly, the peak positions of Ni and Mn were shifted to smaller angles relative to those of Co<sub>3</sub>O<sub>4</sub>, owing to the substitution of Co ions in the native spinel crystal structure, with Ni and Mn ions having different ionic radii. As a result, both the *d*-spacing [the (3 11) orientation was used as an example], and the lattice constants (*a*) increased in the order of Co<sub>3</sub>O<sub>4</sub> < (Ni,Co)<sub>3</sub>O<sub>4</sub> < (Mn,Co)<sub>3</sub>O<sub>4</sub> (Table 1), consistent with observations on other spinel oxides reported in the literature.<sup>[11]</sup> In addition

**Table 1.** The *d*-spacing of (3 11) crystal orientation and lattice constants (*a*) of Co<sub>3</sub>O<sub>4</sub>, (Ni,Co)<sub>3</sub>O<sub>4</sub>, and (Mn,Co)<sub>3</sub>O<sub>4</sub> based on the results obtained from XRD.

Sample	Experimental (311) plane <i>d</i> -spacing [nm]	lattice constant <i>a</i> [Å]	Theoretical (311) plane <i>d</i> -spacing [nm]	lattice constant <i>a</i> [Å]	PDF database Ref.
Co <sub>3</sub> O <sub>4</sub>	0.2439	8.074	0.2437	8.065	#74-2120 (Co <sub>3</sub> O <sub>4</sub> )
(Ni,Co) <sub>3</sub> O <sub>4</sub>	0.2444	8.108	0.2446	8.114	#73-1702 (NiCo <sub>2</sub> O <sub>4</sub> )
(Mn,Co) <sub>3</sub> O <sub>4</sub>	0.2454	8.192	0.2499	8.290	#84-0482 (MnCo <sub>2</sub> O <sub>4</sub> )

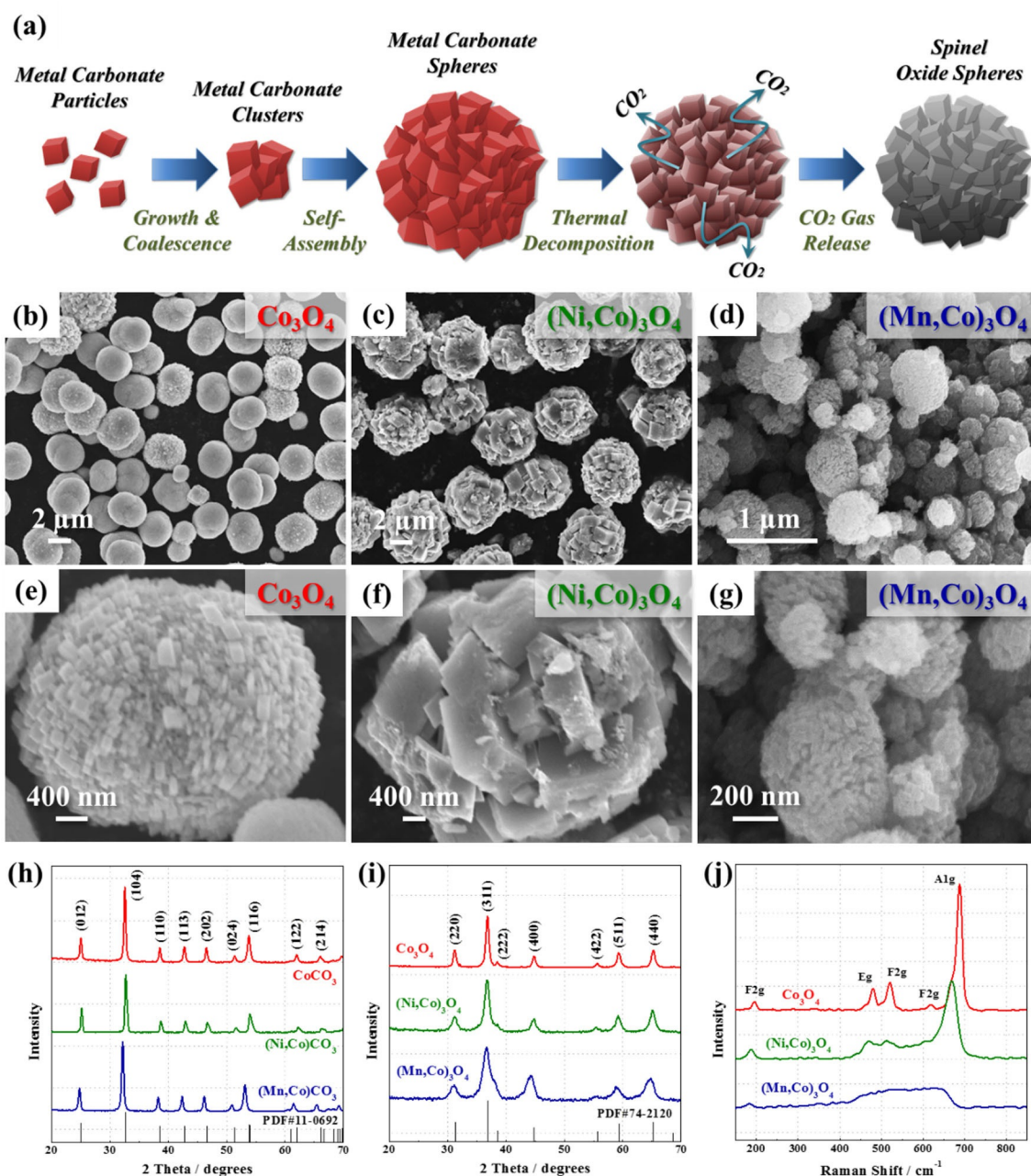


**Figure 1.** (a) Schematic illustration of synthesis of self-assembled mesoporous spinel oxide spheres. SEM images of (b,e)  $\text{Co}_3\text{O}_4$ , (c,f)  $(\text{Ni},\text{Co})_3\text{O}_4$ , and (d,g)  $(\text{Mn},\text{Co})_3\text{O}_4$  mesoporous spheres. XRD patterns obtained (h) before, and (i) after thermal decomposition, and (j) Raman responses of  $\text{Co}_3\text{O}_4$ ,  $(\text{Ni},\text{Co})_3\text{O}_4$ , and  $(\text{Mn},\text{Co})_3\text{O}_4$  mesoporous spheres.

to the XRD analysis, Raman spectroscopy was conducted to confirm the spinel crystal structure, which showed the typical  $F_{2g}$ ,  $E_g$ , and  $A_{1g}$  vibrational modes of  $\text{Co}_3\text{O}_4$  (Figure 1j).<sup>[12]</sup> However, these vibrational modes broadened for  $(\text{Ni},\text{Co})_3\text{O}_4$ , and  $(\text{Mn},\text{Co})_3\text{O}_4$  as a result of less coherent vibrations in mixed transition-metal oxides. To verify the composition of the spinel-oxide spheres, X-ray photoelectron spectroscopy (XPS) was conducted, which confirmed the presence of Co 2p within all three spinel-oxide spheres, in addition to Ni and Mn detected for  $(\text{Ni},\text{Co})_3\text{O}_4$ , and  $(\text{Mn},\text{Co})_3\text{O}_4$ , respectively (Figure 2a). Further XPS analysis of these oxides revealed that the chemical composition at the surface of the mixed-oxide catalysts was

$\text{Ni}_{1.4}\text{Co}_{1.6}\text{O}_4$  and  $\text{Mn}_{1.4}\text{Co}_{1.6}\text{O}_4$ . This suggests that the transition-metal cations occupy both the tetrahedral and octahedral sites. Specifically, de-convoluting the high-resolution Co 2p spectrum of  $\text{Co}_3\text{O}_4$  (777–811 eV) (Figure 2b) revealed splitting of the peak into a  $2p_{1/2}$  (795.0 eV) and  $2p_{3/2}$  (779.8 eV) doublet owing to the presence of cobalt cations with different oxidation states in either the tetrahedral ( $\text{Co}^{\text{II}}$ ) or the octahedral ( $\text{Co}^{\text{III}}$ ) interstitial sites of the spinel lattice.<sup>[13]</sup> Similarly, the de-convoluted Co 2p and Ni 2p spectra (850–890 eV) of  $(\text{Ni},\text{Co})_3\text{O}_4$  (Figure 2c, d), and Co 2p and Mn 2p spectra (637–661 eV) of  $(\text{Mn},\text{Co})_3\text{O}_4$  (Figure 2e, f) showed peak splitting, confirming the presence of both  $\text{M}^{\text{II}}$  and  $\text{M}^{\text{III}}$  oxidation states of the active tran-

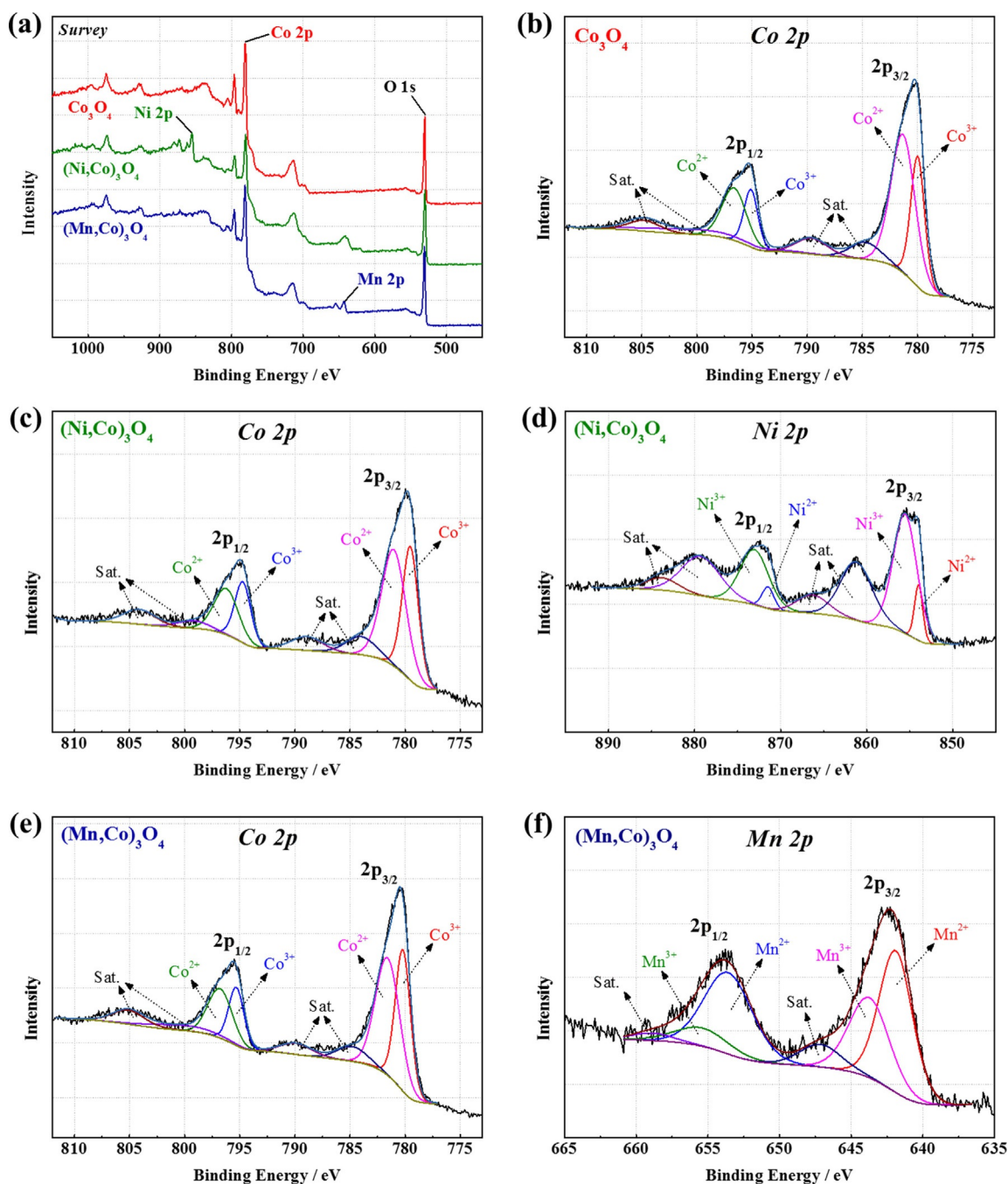


**Figure 2.** (a) Full XPS survey of  $\text{Co}_3\text{O}_4$ ,  $(\text{Ni},\text{Co})_3\text{O}_4$ , and  $(\text{Mn},\text{Co})_3\text{O}_4$ . De-convoluted high-resolution XPS spectra: (b) Co 2p of  $\text{Co}_3\text{O}_4$ ; (c) Co 2p and (d) Ni 2p of  $(\text{Ni},\text{Co})_3\text{O}_4$ ; (e) Co 2p and (f) Mn 2p of  $(\text{Mn},\text{Co})_3\text{O}_4$ .

sition-metal centers. The observation of multiple oxidation states of Co is particularly important for bifunctional catalysis because  $\text{Co}^{\text{II}}$  and  $\text{Co}^{\text{III}}$  are usually considered as the active sites for ORR and OER, respectively.<sup>[7c,14]</sup> The de-convolution of the O 1s spectrum (528–535 eV) obtained for all three spherical oxides showed three peaks that corresponded to oxygen in the spinel lattice, adsorbed  $-\text{OH}$  and  $\text{H}_2\text{O}$ , and surface carbonate anions (Figure S3), most likely owing to residues from the thermal decomposition. The peak splitting of the active transition-metal centers (Co, Ni, and Mn) observed for all three oxides is important, particularly for bifunctional oxygen cataly-

sis, because the multivalent nature of the metal centers in the spinel structure was consistently reported to allow rapid charge transfer through electron hopping as well as improved interaction with oxygen intermediates during the oxygen reactions.<sup>[13]</sup>

After characterization of the physical properties of the spinel-oxide spheres, their electrochemical activities towards bifunctional ORR and OER were evaluated by half-cell rotating disk electrode (RDE) voltammetry at various rotation speeds (Figure S4). Based on the ORR polarization curves obtained at 1600 rpm in  $\text{O}_2$ -saturated 0.1 M KOH (Figure 3a),  $(\text{Ni},\text{Co})_3\text{O}_4$  ap-

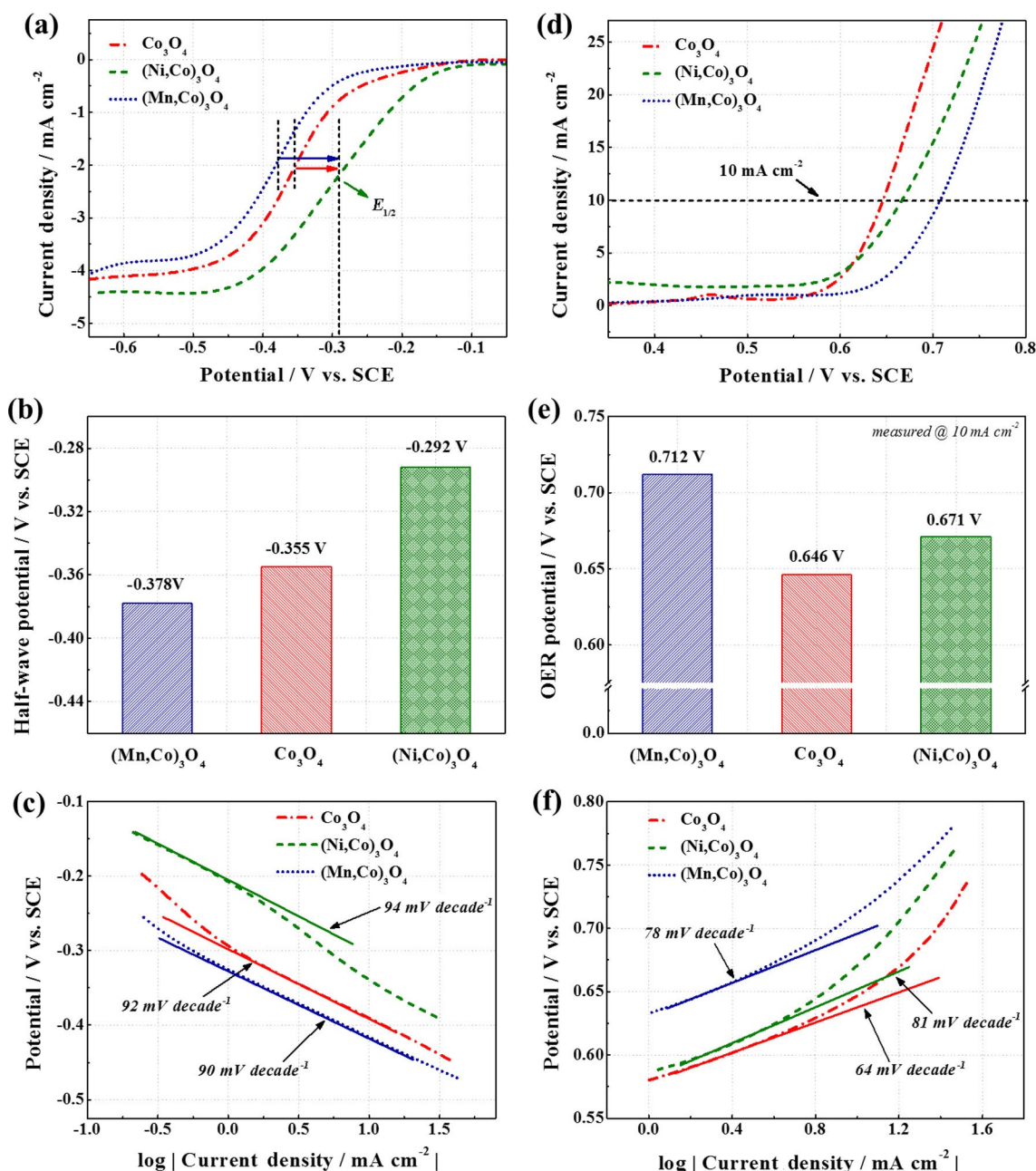


**Figure 3.** (a) ORR polarization curves obtained by RDE voltammetry at rotation rate of 1600 rpm in  $\text{O}_2$ -saturated  $0.1 \text{ M KOH}$ . (b) Comparison of half-wave potentials. (c) ORR Tafel slopes. (d) OER CV curves obtained in  $\text{N}_2$ -saturated  $0.1 \text{ M KOH}$ . (e) Comparison of OER potentials at  $10 \text{ mA cm}^{-2}$ . (f) OER Tafel slopes of  $\text{Co}_3\text{O}_4$ ,  $(\text{Ni,Co})_3\text{O}_4$ , and  $(\text{Mn,Co})_3\text{O}_4$ .

peared to be significantly positive-shifted, indicative of superior ORR activity, followed by  $\text{Co}_3\text{O}_4$  and  $(\text{Mn,Co})_3\text{O}_4$ . In particular,  $(\text{Ni,Co})_3\text{O}_4$  demonstrated a positive onset potential [ $-0.127 \text{ V}$  vs. saturated calomel electrode (SCE)] compared to those of  $\text{Co}_3\text{O}_4$  and  $(\text{Mn,Co})_3\text{O}_4$  ( $-0.171$  and  $-0.217 \text{ V}$ , respectively). This signifies a lower activation energy required for  $(\text{Ni,Co})_3\text{O}_4$  to overcome the barrier of the first electron reaction, which is considered to be the rate-limiting step. The same trend was observed with the half-wave potentials ( $E_{1/2}$ ),  $(\text{Ni,Co})_3\text{O}_4$  demonstrating the most positively shifted  $E_{1/2}$  of  $-0.292 \text{ V}$  compared to  $-0.355$  and  $-0.378 \text{ V}$  for  $\text{Co}_3\text{O}_4$  and  $(\text{Mn,Co})_3\text{O}_4$ , respectively (Figure 3b). Further investigation by Tafel analysis re-

vealed that the three oxides showed comparable slopes in the range of  $90\text{--}94 \text{ mV decade}^{-1}$  (Figure 3c), which suggests that the ORR on these catalysts proceeded at similar rates even though the energy requirements for overcoming the first electron reaction are different. As such, introducing active metal substituents (Ni, Mn) into the pristine  $\text{Co}_3\text{O}_4$  spinel lattice affects mostly the degree of binding with oxygen and the formation of first reduced oxygen species,<sup>[15]</sup> whereas the rest of the intermediate reactions proceed at similar kinetic rates.

In addition to the ORR activity, the OER activity of the spinel oxides was evaluated, showing that  $(\text{Ni,Co})_3\text{O}_4$  and  $\text{Co}_3\text{O}_4$  had very similar onset potentials ( $\approx 0.60 \text{ V}$ ) and  $(\text{Mn,Co})_3\text{O}_4$  a more

positive-shifted (less active) onset potential (0.65 V) (Figure 3d). Despite the similar onset potentials,  $\text{Co}_3\text{O}_4$  resulted in a slightly more negative (more active) OER potential ( $E_{\text{OER}}$ ) of 0.646 V measured at  $10 \text{ mA cm}^{-2}$  compared to those of  $(\text{Ni},\text{Co})_3\text{O}_4$  and  $(\text{Mn},\text{Co})_3\text{O}_4$  (0.671 and 0.712 V, respectively; Figure 3e). The OER Tafel analysis of  $\text{Co}_3\text{O}_4$  resulted in the lowest slope of  $64 \text{ mV decade}^{-1}$ , followed by 81 and  $78 \text{ mV decade}^{-1}$  obtained with  $(\text{Ni},\text{Co})_3\text{O}_4$  and  $(\text{Mn},\text{Co})_3\text{O}_4$ , respectively (Figure 3f), which is indicative of more rapid OER kinetics for  $\text{Co}_3\text{O}_4$  despite an onset potentials similar to that of  $(\text{Ni},\text{Co})_3\text{O}_4$ . For both ORR and OER, the relatively lower activity and slower kinetics observed for  $(\text{Mn},\text{Co})_3\text{O}_4$  were most likely a result of its least favorable interaction with oxygen intermediates owing to lattice expansion and broadened vibrational modes (as observed by XRD and Raman analyses, respectively).

The differences in the ORR and OER activities of the metal oxides also suggest that they are clearly dependent on the type of transition-metal substituent inserted into the spinel-oxide structure. To confirm this, double-layer capacitance was measured as the slope of current versus scan rate obtained by conducting cyclic voltammetry at various scan rates in a potential window in which no Faradaic redox reactions occur (Figure S5). The double-layer capacitance was reported to be linearly proportional to the electrochemically active surface area (ECSA) of metal oxides.<sup>[16]</sup> Interestingly, the measured capacitance values of 2.9, 2.6, and  $4.4 \text{ mF cm}^{-2}$  obtained with  $\text{Co}_3\text{O}_4$ ,  $(\text{Ni},\text{Co})_3\text{O}_4$ , and  $(\text{Mn},\text{Co})_3\text{O}_4$ , respectively, show the same trend as the BET surface areas [ $(\text{Ni},\text{Co})_3\text{O}_4 < \text{Co}_3\text{O}_4 < (\text{Mn},\text{Co})_3\text{O}_4$ ], confirming the validity of the surface areas measured in this study. The differences in the surface area of the metal oxides, however, were found to have a less dominant effect on the catalytic activity for ORR and OER compared to the compositional effect demonstrated by introducing Ni and Mn transition-metal substituents into the spinel-oxide structure. This led to  $(\text{Ni},\text{Co})_3\text{O}_4$  demonstrating the smallest potential difference between ORR and OER despite exhibiting the smallest BET surface area and double-layer capacitance. Specifically,  $(\text{Ni},\text{Co})_3\text{O}_4$  showed the best overall bifunctional catalytic activity with the smallest potential difference ( $\Delta E_{\text{OER-ORR}} = 1.01 \text{ V}$ ) between the ORR and OER potentials measured at current densities of  $-3$  and  $10 \text{ mA cm}^{-2}$ , respectively (Table S1). Based on a literature survey, the ORR/OER potential difference was found to be smaller in comparison to many reports and even comparable to some of the best published results on non-precious transition-metal-oxide-based bifunctional catalysts. The activity enhancement is attributed to the insertion of Ni cations into the octahedral sites of the spinel lattice, which has been reported to improve the electrical conductivity of the spinel oxide.<sup>[17]</sup>

In contrast, the catalytic activity of  $\text{Co}_3\text{O}_4$  largely favors OER, leading to a reduced OER overpotential and the generation of high current densities. This is attributed to relatively weak adsorption energy between oxygen adsorbate and the surface of active Co cations, promoting the release of oxygen during OER.<sup>[18]</sup> This concomitantly reduces the ORR activity owing to the weak binding and insufficient energy to activate adsorbed oxygen. The high bifunctional catalytic activities of the spinel-oxide spheres, in comparison to a commercially available

$\text{Co}_3\text{O}_4$ -nanoparticle catalyst, are highlighted by considerably improved ORR (positive-shifted) and OER (negative-shifted) potentials (Figure S6). However, in comparison to a mixture of the precious-metal benchmark catalysts Pt/C and Ir/C, the spinel-oxide spheres showed comparatively weaker bifunctional activity. This sacrificed activity is currently the main disadvantage caused by utilizing inexpensive non-precious transition-metal-based catalysts as opposed to precious metals, and can be minimized by hybridizing with nanostructured active carbon to synergistically improve both ORR and OER performances.

To provide further insight into the bifunctional electrochemical behavior of the spinel oxides, first-principles DFT calculations were conducted by modeling their cubic  $Fd3m$  space-group lattice in a periodic two-layer slab with a  $(2 \times 2)$  unit cell (Figure S7). In the spinel lattices of  $(\text{Ni},\text{Co})_3\text{O}_4$  and  $(\text{Mn},\text{Co})_3\text{O}_4$ , Ni and Mn ions are known to preferentially occupy the octahedral interstitial sites, whereas Co ions are distributed over both octahedral and tetrahedral sites. Therefore,  $(\text{Ni},\text{Co})_3\text{O}_4$  and  $(\text{Mn},\text{Co})_3\text{O}_4$  were modeled by exchanging half of the octahedral Co ions with Ni or Mn in  $\text{Co}_3\text{O}_4$ .<sup>[9]</sup> During ORR and OER, the metal-oxide surfaces undergo changes owing to the interaction with different oxygen intermediates (i.e.,  $^*\text{OOH}$ ,  $^*\text{O}$ , and  $^*\text{OH}$ ; Figure 4a–c, respectively). The band diagram shows the changes in the Gibbs free energy ( $\Delta G$ ) of the spinel oxides during interaction with each of these intermediates at zero potential ( $U = 0 \text{ V}$ ), equilibrium potential ( $U = 1.23 \text{ V}$ ), and the potential at which all oxygen intermediates proceed spontaneously (Figure 4d–f). Based on these band-energy calculations, the limiting thermodynamic potential at which all steps proceed downward was calculated to be  $U = 0.14$  and  $0.66 \text{ V}$  for  $\text{Co}_3\text{O}_4$  and  $(\text{Ni},\text{Co})_3\text{O}_4$ , respectively. However, with  $(\text{Mn},\text{Co})_3\text{O}_4$ , the energy of the intermediate reaction corresponding to the reduction of  $\text{OH}^*$  to  $\text{OH}^-$  remained slightly thermodynamically upward even at  $U = 0 \text{ V}$ . These calculations predicted the degree of ORR activity for the spinel oxides to be in the order of  $(\text{Mn},\text{Co})_3\text{O}_4 < \text{Co}_3\text{O}_4 < (\text{Ni},\text{Co})_3\text{O}_4$ , which parallels the activity trends observed experimentally (Figure 5a). Specifically,  $(\text{Ni},\text{Co})_3\text{O}_4$ , with the highest  $U$  potential, showed the most positively shifted onset and half-wave ORR potentials, whereas the lower  $U$  potential of  $\text{Co}_3\text{O}_4$  corresponded to relatively negative-shifted ORR potentials. Lastly, the lowest  $U$  potential obtained with  $(\text{Mn},\text{Co})_3\text{O}_4$  was in agreement with the even further negative-shifted ORR potentials obtained experimentally.

To predict the OER activities of the spinel oxides, potentials higher than  $1.23 \text{ V}$  were applied to find the point at which all free energies associated with OER intermediate reactions proceeded spontaneously, resulting in  $U = 2.09$ ,  $2.26$ , and  $2.93 \text{ V}$  obtained with  $\text{Co}_3\text{O}_4$ ,  $(\text{Ni},\text{Co})_3\text{O}_4$ , and  $(\text{Mn},\text{Co})_3\text{O}_4$ , respectively. The lowest  $U$  potential of  $\text{Co}_3\text{O}_4$  is an indication that it exhibits superior OER activity, followed by  $(\text{Ni},\text{Co})_3\text{O}_4$  and  $(\text{Mn},\text{Co})_3\text{O}_4$ . These DFT predictions are also in good agreement with the OER potentials obtained experimentally at  $10 \text{ mA cm}^{-2}$  (Figure 5b). The fact that  $\text{Co}_3\text{O}_4$  outperformed  $(\text{Ni},\text{Co})_3\text{O}_4$  despite the relatively smaller activity difference (as well as  $U$  potential difference) suggests that the adsorption strength between oxygen intermediates and active metal cations has a greater

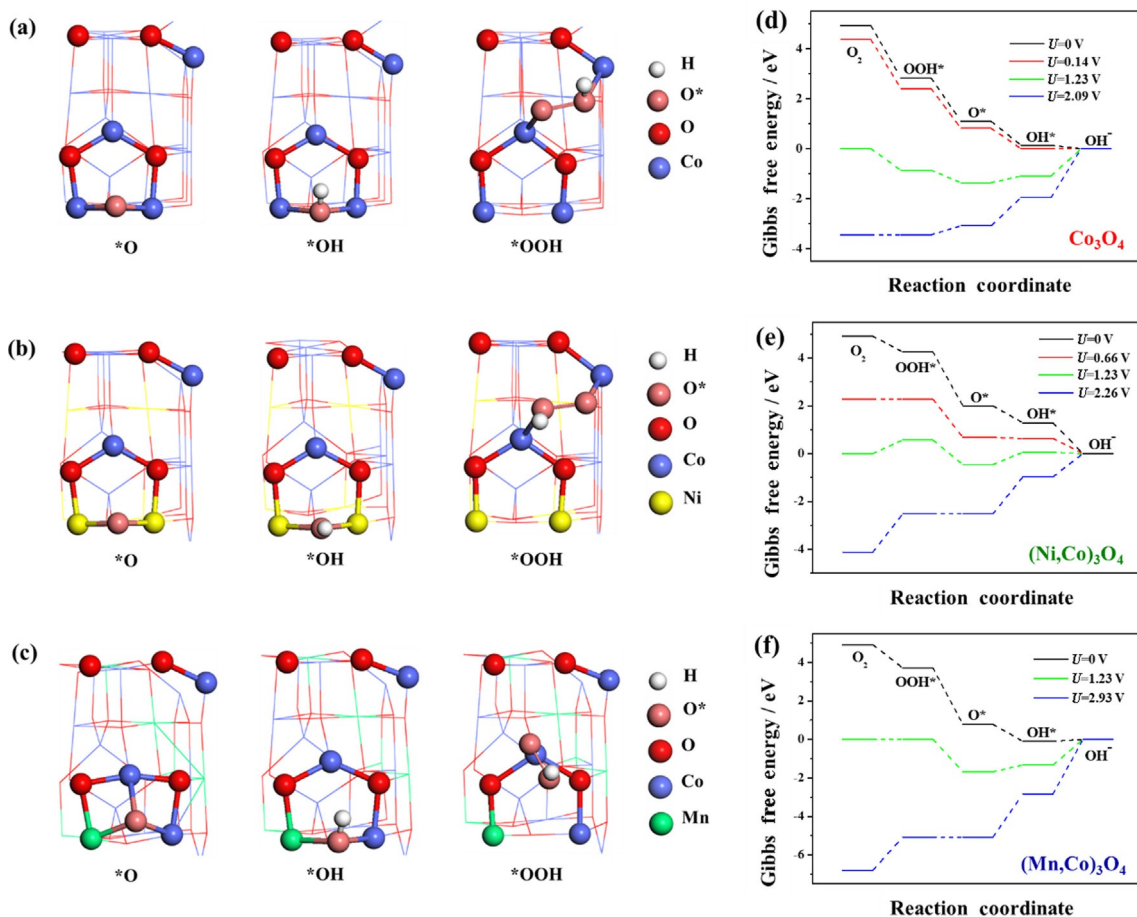


**Figure 4.** Periodic six-atomic-layer slabs with a  $(2 \times 2)$  unit cell of (a)  $\text{Co}_3\text{O}_4$ , (b)  $(\text{Ni,Co})_3\text{O}_4$ , and (c)  $(\text{Mn,Co})_3\text{O}_4$ , depicting interaction between oxygen intermediates and the catalyst surface during ORR/OER. (d–f) Standard free-energy band diagrams obtained at zero potential ( $U=0\text{ V}$ ), equilibrium potential ( $U=1.23\text{ V}$ ), and the potential at which all intermediates proceed spontaneously at pH 14 and  $T=298\text{ K}$ . All potentials are indicated vs. reversible hydrogen electrode (RHE) unless otherwise noted.

effect on the overall OER activity than the electrical conductivity enhancement. Because OER is the reverse reaction of ORR,  $\text{Co}_3\text{O}_4$ , which demonstrated a lower ORR activity owing to weaker adsorption with oxygen can be expected to more readily release oxygen during OER.  $(\text{Mn,Co})_3\text{O}_4$ , having demonstrated the least ORR and OER activities, likely stabilizes oxygen intermediates to the extent that they become inactive for the reactions. However,  $(\text{Mn,Co})_3\text{O}_4$  can still be deemed a suitable catalyst for less energy-intensive applications because the abundance of Mn makes it a much more cost-competitive alternative to Co.

## Conclusions

In this study, spinel-oxide-structured nanocrystals self-assembled into mesoporous spheres were synthesized as bifunctional catalysts active for the oxygen reduction reaction (ORR) and oxygen evolution reaction (OER). Experimentally, an increasing ORR activity was observed in the order of  $(\text{Mn,Co})_3\text{O}_4 < \text{Co}_3\text{O}_4 < (\text{Ni,Co})_3\text{O}_4$  in terms of onset and half-wave potentials, whereas increasing OER activity was observed in the order of  $(\text{Mn,Co})_3\text{O}_4 < (\text{Ni,Co})_3\text{O}_4 < \text{Co}_3\text{O}_4$  in terms of potential measured

at the current density of  $10\text{ mA cm}^{-2}$ . The first-principles DFT analysis of the catalysts revealed the same activity trends for both ORR and OER based on the Gibbs free energies obtained at the potential for which all intermediate reactions occur spontaneously. The superior ORR activity of  $(\text{Ni,Co})_3\text{O}_4$  is attributed to the enhanced electrical conductivity owing to the insertion of Ni ions into the octahedral interstitials of the spinel lattice, which promotes rapid charge transfer during the electrocatalytic reaction. The superior OER activity of  $\text{Co}_3\text{O}_4$  is attributed to favorable adsorption strength between oxygen intermediates and active Co cations, facilitating rapid release of evolved oxygen. In contrast,  $(\text{Mn,Co})_3\text{O}_4$  demonstrated relatively lower ORR and OER activities, most likely owing to lattice expansion and incoherent vibrational modes observed by XRD and Raman analyses, respectively, which result in over-stabilization and deactivation of the oxygen intermediates. The relationship between the composition of spinel-oxide catalysts and the degree of ORR and OER activities investigated in this study by both experimental and computational analysis provides an excellent selection criterion for appropriately choosing a bifunctional catalyst based on the energy requirements of specific applications.

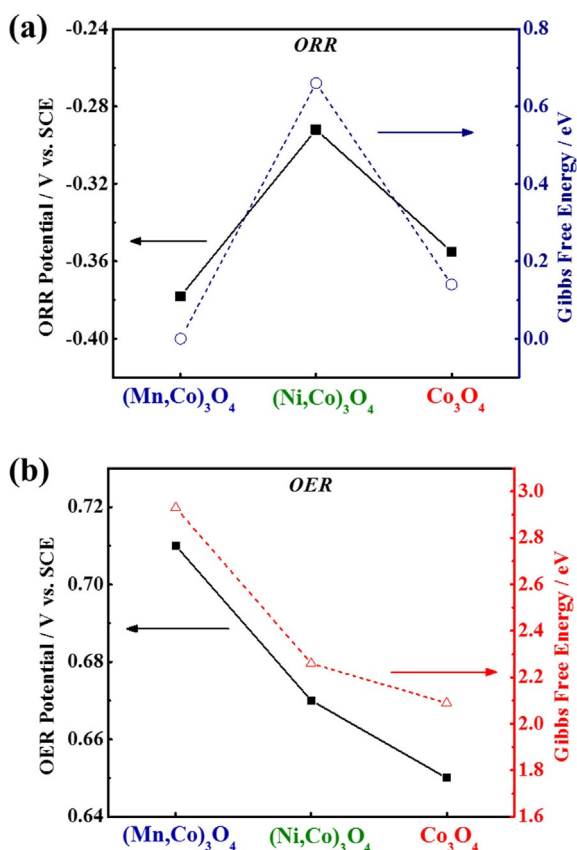


**Figure 5.** Comparisons of (a) ORR half-wave potentials and (b) OER potentials measured at  $10 \text{ mA cm}^{-2}$  obtained experimentally with Gibbs free energies from DFT computational analysis of  $\text{Co}_3\text{O}_4$ ,  $(\text{Ni,Co})_3\text{O}_4$ , and  $(\text{Mn,Co})_3\text{O}_4$ .

## Experimental Section

### Synthesis of metal-oxide spheres

The metal-oxide spheres were prepared by a facile solvothermal technique, for which cobalt nitrate hexahydrate [3.0 mmol; 2:1 mass ratio of cobalt nitrate hexahydrate and either nickel nitrate hexahydrate or manganese nitrate tetrahydrate for the synthesis of  $(\text{Ni,Co})_3\text{O}_4$  or  $(\text{Mn,Co})_3\text{O}_4$ ] was dissolved in a mixed solution of ethylene glycol (30 mL) and double de-ionized (DDI) water (10 mL) by stirring for 30 min. Then, ammonium bicarbonate (30 mmol) was added to the mixture and dissolved by stirring for 30 min. The solution was then transferred to a Teflon cup inside a stainless-steel autoclave reactor and heated in the oven at  $200^\circ\text{C}$  for 24 h. The resulting solid product was centrifuged five times, three times with DDI water and two times with ethanol, and then dried overnight in a  $60^\circ\text{C}$  oven. Finally, the dried product was calcined using a furnace in air at  $350^\circ\text{C}$  for 2 h.

### Physical characterization

The metal-oxide spheres synthesized in this study were characterized by the following techniques. SEM (LEO FESEM 1530) was used to analyze morphology and surface topology of the materials. A surface-area and porosity analyzer (Quantachrome Instruments QuadraSorb SI4) was used to obtain nitrogen absorption-desorption isotherms for calculating the BET surface area, and the BJH model was used to obtain pore-size distributions. XRD (Bruker AXS D8 Advance), Raman spectroscopy (Thermo Fisher Scientific DXR

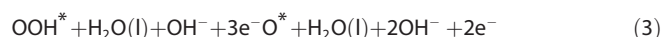
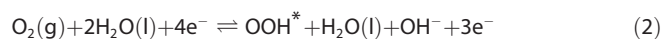
Raman Microscope), and XPS (Thermo Scientific K-Alpha XPS spectrometer) were used to confirm the crystal structure, vibrational modes, and elemental composition, respectively.

### Electrochemical evaluation

The half-cell electrochemical evaluation of the metal oxides was conducted with RDE voltammetry using a three-electrode glass cell, potentiostat (CH Instruments 760D), and rotation speed controller (Pine Instruments Co., AFMSRCE). To prepare the working electrode, the ink solution prepared by mixing metal oxide and carbon black (Vulcan Carbon XC-72) in a 1:1 mass ratio in an ethanol-diluted AS-4 (Tokuyama Corp.) ionomer solution with a total active-material concentration of  $4 \text{ mg mL}^{-1}$  was coated onto a polished glassy carbon disk electrode (5 mm OD), resulting in active-material loading of  $0.20 \text{ mg cm}^{-2}$ . As the counter and reference electrodes, a platinum wire and SCE were used, respectively, and 0.1 M KOH was used as the electrolyte. To activate the working electrode, cyclic voltammetry was conducted for 20 cycles at a scan rate of  $50 \text{ mV s}^{-1}$ , and the background current was measured at a scan rate of  $10 \text{ mV s}^{-1}$  within the potential range of 0 to  $-1.0 \text{ V vs. SCE}$  in the  $\text{N}_2$ -saturated electrolyte. The oxygen reduction and oxygen evolution activities were then measured in the oxygen- and nitrogen-saturated electrolyte, respectively, at a scan rate of  $10 \text{ mV s}^{-1}$ . To measure double-layer capacitance, cyclic voltammetry of the working electrode was obtained at various scan rates (2.5, 5, 10, 20, and  $40 \text{ mV s}^{-1}$ ) over a potential window of 60 mV around the open-circuit potential in a 0.1 M solution of tetrabutylammonium hexafluorophosphate in acetonitrile.

### Computational details

DFT calculations were performed using the program BAND<sup>[19]</sup>, in which the electron wave functions were developed on a basis set of numerical atomic orbitals (NAOs) and Slater-type orbitals (STOs). The triple polarization (TZP) basis of Slater-type orbitals was used. The calculations were performed by using Revised Perdew-Burke-Ernzerhof (RPBE) generalized gradient approximation (GGA) for the exchange and correlation energy terms.<sup>[20]</sup> This is a widely accepted function for various applications, including metal-oxide systems, producing reliable energetics.<sup>[21]</sup> The BAND program performs numerical integrations for all matrix elements.<sup>[22]</sup> The accuracy of the integration in real space (*Accuracy*) and the sampling of the Brillouin zone (*k-space*) for the integration accuracy in *k-space* are two key major numerical parameters in the present DFT calculations. In the present study, the *Accuracy* parameter was set to 4, which is a reasonable value based on previous analysis,<sup>[15,23]</sup> whereas the *k-space* parameter was set to 3,<sup>[17,24]</sup> which indicates that the quadratic tetrahedron method<sup>[25]</sup> was chosen to perform the *k-space* numerical integration. The calculations performed on this study were spin-unrestricted. For modelling, the ORR/OER behaviors were predicted on the (110) surface of the spinel crystal using periodic six atomic-layer slabs with a  $(2 \times 2)$  unit cell. The (110) surface was chosen because it was predicted to be one of the most stable planes exposed in a number of cubic spinel  $\text{Co}_3\text{O}_4$  specimens prepared by various methods.<sup>[26]</sup> The bottom two atomic layers of the slab were fixed in their bulk positions, whereas the remaining atomic layers and the adsorbed species were set free to relax. On the basis of fully relaxed structures, the free energy of each oxygen-intermediate reaction ( $\Delta G$ ) during ORR/OER on  $\text{Co}_3\text{O}_4$ ,  $(\text{Ni,Co})_3\text{O}_4$ , and  $(\text{Mn,Co})_3\text{O}_4$  surfaces was calculated. Specifically, the following oxygen-intermediate reactions were considered for alkaline electrolyte conditions expressed in terms of  $\text{OH}^-$  [Eqs. (2)–(5)]:



Using the expression for  $\Delta G$  defined as the following Equation (6)

$$\Delta G = \Delta E + \Delta \text{ZPE} - T\Delta S \quad (6)$$

in which  $\Delta E$ ,  $\Delta \text{ZPE}$ , and  $\Delta S$  represent the difference in the DFT-calculated ground-state energy, zero-point energy, and entropy corrections, respectively, the free energy of each intermediate reaction was calculated. As an example, the free energy of reaction (2) ( $\Delta G_2$ ) was calculated as a function of the reversible potential  $U^0$  using the following Equations (7) and (8):

$$\Delta G_2 = \Delta G_{\text{OOH}^*} - \Delta G_{\text{O}_2\text{g}} - 1/2\Delta G_{\text{H}_2} - kT \ln a_{\text{H}^+} + eU^0 \quad (7)$$

$$\Delta G_{\text{OOH}^*} = \Delta E_{\text{OOH}^*} + \Delta \text{ZPE}_{\text{OOH}^*} - T\Delta S_{\text{OOH}^*} \quad (8)$$

The values of  $\Delta \text{ZPE}$  used and further details of the free-energy calculation can be found in the previously published references.<sup>[15,27]</sup>

## Acknowledgements

This work was conducted under framework of the research and development program of KIER (B7-2425) from Republic of Korea, and made possible by access to the facilities of the Shared Hierarchical Academic Research Computing Network (SHARCNET: www.sharcnet.ca) and Compute/Calcul Canada, and by the Natural Sciences and Engineering Research Council of Canada (NSERC) grants provided to Z.C. and the University of Waterloo.

## Conflict of interest

The authors declare no conflict of interest.

**Keywords:** bifunctional catalysts • density functional theory • oxygen evolution • oxygen reduction • spinel oxides

- [1] a) M. A. Rahman, X. Wang, C. Wen, *J. Electrochem. Soc.* **2013**, *160*, A1759–A1771; b) J. S. Lee, S. Tai Kim, R. Cao, N. S. Choi, M. Liu, K. T. Lee, J. Cho, *Adv. Energy Mater.* **2011**, *1*, 34–50; c) F. Cheng, J. Chen, *Chem. Soc. Rev.* **2012**, *41*, 2172–2192; d) D. U. Lee, J.-Y. Choi, K. Feng, H. W. Park, Z. Chen, *Adv. Energy Mater.* **2014**, *4*, 1301389.
- [2] D. U. Lee, P. Xu, Z. P. Cano, A. G. Kashkooli, M. G. Park, Z. Chen, *J. Mater. Chem. A* **2016**, *4*, 7107–7134.
- [3] a) D. U. Lee, H. W. Park, M. G. Park, V. Ismayilov, Z. Chen, *ACS Appl. Mater. Interfaces* **2015**, *7*, 902–910; b) H. W. Park, D. U. Lee, P. Zamani, M. H. Seo, L. F. Nazar, Z. Chen, *Nano Energy* **2014**, *10*, 192–200; c) D. U. Lee, J. Scott, H. W. Park, S. Abureden, J.-Y. Choi, Z. Chen, *Electrochem. Commun.* **2014**, *43*, 109–112.

- [4] a) L. Tao, Q. Wang, S. Dou, Z. Ma, J. Huo, S. Wang, L. Dai, *Chem. Commun.* **2016**, *52*, 2764–2767; b) D. U. Lee, B. J. Kim, Z. Chen, *J. Mater. Chem. A* **2013**, *1*, 4754–4762.
- [5] a) Y. J. Sa, K. Kwon, J. Y. Cheon, F. Kleitz, S. H. Joo, *J. Mater. Chem. A* **2013**, *1*, 9992–10001; b) M. Risch, K. A. Stoerzinger, S. Maruyama, W. T. Hong, I. Takeuchi, Y. Shao-Horn, *J. Am. Chem. Soc.* **2014**, *136*, 5229–5232.
- [6] a) G. L. Tian, Q. Zhang, B. Zhang, Y. G. Jin, J. Q. Huang, D. S. Su, F. Wei, *Adv. Funct. Mater.* **2014**, *24*, 5956–5961; b) Z. Lin, G. H. Waller, Y. Liu, M. Liu, C.-p. Wong, *Nano Energy* **2013**, *2*, 241–248; c) B. Y. Xia, Y. Yan, N. Li, H. B. Wu, X. W. D. Lou, X. Wang, *Nat. Energy* **2016**, *1*, 15006.
- [7] a) Z. Chen, A. Yu, D. Higgins, H. Li, H. Wang, Z. Chen, *Nano Lett.* **2012**, *12*, 1946–1952; b) Z. Wang, Y. Lu, Y. Yan, T. Y. P. Larissa, X. Zhang, D. Wu, H. Zhang, Y. Yang, X. Wang, *Nano Energy* **2016**, *30*, 368–378; c) J. Wang, X. Ge, Z. Liu, L. Thia, Y. Yan, W. Xiao, X. Wang, *J. Am. Chem. Soc.* **2017**, *139*, 1878–1884.
- [8] D. U. Lee, M. G. Park, H. W. Park, M. H. Seo, X. Wang, Z. Chen, *ChemSusChem* **2015**, *8*, 3129–3138.
- [9] H.-P. Cong, S.-H. Yu, *Cryst. Growth Des.* **2009**, *9*, 210–217.
- [10] M. G. Park, D. U. Lee, M. H. Seo, Z. P. Cano, Z. Chen, *Small* **2016**, *12*, 2707–2714.
- [11] a) E. Castro, C. Gervasi, *Int. J. Hydrogen Energy* **2000**, *25*, 1163–1170; b) C. Fu, G. Li, D. Luo, X. Huang, J. Zheng, L. Li, *ACS Appl. Mater. Interfaces* **2014**, *6*, 2439–2449.
- [12] J. Yang, H. Liu, W. N. Martens, R. L. Frost, *J. Phys. Chem. C* **2010**, *114*, 111–119.
- [13] M. Hamdani, R. N. Singh, P. Chartier, *Int. J. Electrochem. Sci.* **2010**, *5*, 556–577.
- [14] T. W. Kim, M. A. Woo, M. Regis, K.-S. Choi, *J. Phys. Chem. Lett.* **2014**, *5*, 2370–2374.
- [15] M. H. Seo, H. W. Park, D. U. Lee, M. G. Park, Z. Chen, *ACS Catal.* **2015**, *5*, 4337–4344.
- [16] a) L. Yu, B. Y. Xia, X. Wang, X. W. Lou, *Adv. Mater.* **2016**, *28*, 92–97; b) C. C. McCrory, S. Jung, J. C. Peters, T. F. Jaramillo, *J. Am. Chem. Soc.* **2013**, *135*, 16977–16987; c) J. A. Koza, Z. He, A. S. Miller, J. A. Switzer, *Chem. Mater.* **2012**, *24*, 3567–3573.
- [17] Y. Li, P. Hasin, Y. Wu, *Adv. Mater.* **2010**, *22*, 1926–1929.
- [18] J. Greeley, I. Stephens, A. Bondarenko, T. P. Johansson, H. A. Hansen, T. Jaramillo, J. Rossmeisl, I. Chorkendorff, J. K. Nørskov, *Nat. Chem.* **2009**, *1*, 552–556.
- [19] G. Wiesenekker, E. Baerends, *J. Phys. Condens. Matter* **1991**, *3*, 6721.
- [20] J. P. Perdew, K. Burke, M. Ernzerhof, *Phys. Rev. Lett.* **1996**, *77*, 3865.
- [21] a) Q. Zhang, Y. Wang, Z. W. Seh, Z. Fu, R. Zhang, Y. Cui, *Nano Lett.* **2015**, *15*, 3780–3786; b) X.-Q. Gong, Z.-P. Liu, R. Raval, P. Hu, *J. Am. Chem. Soc.* **2004**, *126*, 8–9.
- [22] G. Te Velde, E. Baerends, *J. Comput. Phys.* **1992**, *99*, 84–98.
- [23] a) J. Li, E. Croiset, L. Ricardez-Sandoval, *Chem. Phys. Lett.* **2015**, *639*, 205–210; b) J. Li, E. Croiset, L. Ricardez-Sandoval, *J. Phys. Chem. C* **2013**, *117*, 16907–16920.
- [24] J. Li, E. Croiset, L. Ricardez-Sandoval, *Phys. Chem. Chem. Phys.* **2014**, *16*, 2954–2961.
- [25] G. Wiesenekker, G. Te Velde, E. Baerends, *J. Phys. C* **1988**, *21*, 4263.
- [26] a) F. Zasada, J. Grybos, P. Indyka, W. Piskorz, J. Kaczmarczyk, Z. Sojka, *J. Phys. Chem. C* **2014**, *118*, 19085–19097; b) F. Kapteijn, J. Rodriguez-Mirasol, J. A. Moulijn, *Appl. Catal. B* **1996**, *9*, 25–64; c) X. Liu, G. Qiu, X. Li, *Nanotechnology* **2005**, *16*, 3035.
- [27] J. K. Nørskov, J. Rossmeisl, A. Logadottir, L. Lindqvist, J. R. Kitchin, T. Bligaard, H. Jonsson, *J. Phys. Chem. B* **2004**, *108*, 17886–17892.

Manuscript received: February 27, 2017

Revised: March 24, 2017

Accepted Article published: March 29, 2017

Final Article published: April 24, 2017